June 2011

Supplemental Material for: "Improved sea ice shortwave radiation physics in CCSM4: The impact of melt ponds and aerosols on Arctic sea ice"

Marika Holland, David A. Bailey, Bruce P. Briegleb

Bonnie Light and Elizabeth Hunke

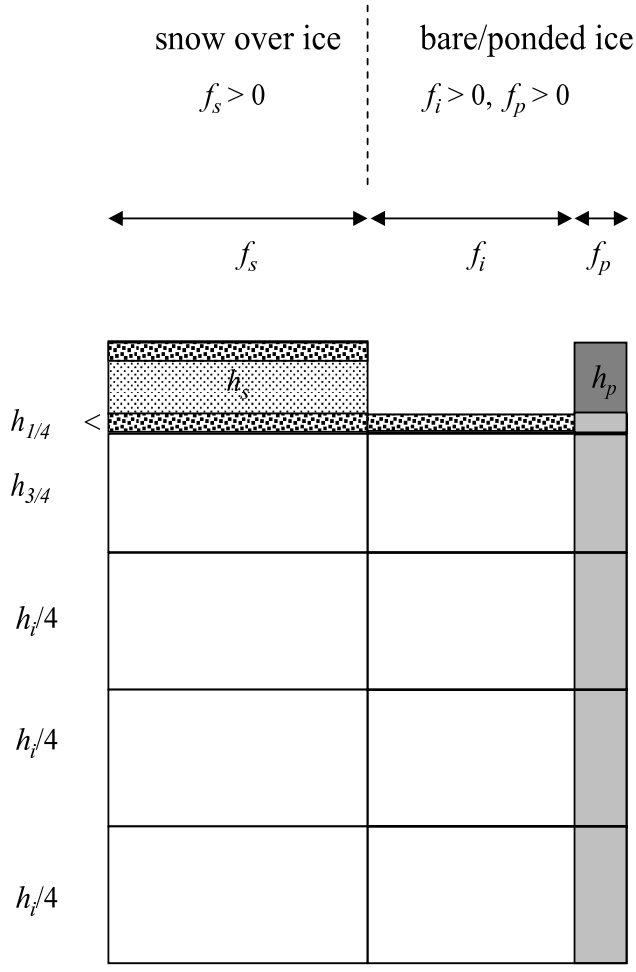

Introduction

This Supplemental Material supports the paper: Improved sea ice shortwave radiation physics in CCSM4: The impact of melt ponds and black carbon, by Marika Holland, David A. Bailey, Bruce P. Briegleb, Bonnie Light and Elizabeth Hunke.

Part A presents detailed algorithms used in CCSM4 sea ice shortwave, while Part B presents a detailed comparison of computed albedos against Antarctic snow and sea ice measurments from Brandt et. al (2005).

A. CCSM4 Sea Ice Shortwave Algorithms

Here we provide a summary of the numerical algorithms and necessary optical properties for the Delta-Eddington Shortwave Parameterization. For a detailed discussion (in particular derivations and validations), see Briegleb and Light (2007), NCAR Tech Note, TN-472+STR, 100pp.

Four separate shortwave (SW) or solar radiation fluxes are provided to the sea ice surface, divided by spectral band: visible (vs) $0.2 - 0.7$ μm, near-infrared (ni) $0.7 - 5.00$ μm, and angularly: direct solar beam (dr) and diffuse (df). The sum of these band and angle fluxes is the total downwelling shortwave radiation (F_{SWDN}) incident on the sea ice surface:

$$F_{SWDN} = F_{SWvsdr} + F_{SWvsdf} + F_{SWnidr} + F_{SWnidf}. \quad (A1)$$

Additionally, we characterize the direct solar beam by the cosine of the solar zenith angle μ_0 $(0 < \mu_0 \leq 1)$, with $\mu_0 = +1$ for overhead sun.

We consider the total sea ice surface in a grid box to be separable into three distinct horizontally homogeneous types: snow over sea ice, bare sea ice and pond over sea ice (or ponded sea ice), as shown in Fig A1. These surface types are characterized by aeral fractions f_s, f_i and f_p respectively, such that over the entire sea ice horizontal surface in a grid box:

$$f_s + f_i + f_p = 1 \quad (A2)$$

Fig A1 additionally shows the vertical structure of these surfaces: a single snow or pond layer (if present), of physical depths h_s and h_p respectively, above sea ice of physical thickness h_i divided evenly into four equal thickness ($h_i/4$) layers. Furthermore, the top layer in sea ice, as well as the snow layer, is subdivided into a surface scattering (granular) sublayer (SSL) of thickness $h_{1/4}$ in sea ice and a drained layer (DL) of thickness $h_{3/4}$ in sea ice, such that $h_{1/4} + h_{3/4} = h_i/4$. The three remaining layers in sea ice are refered to as interior layers (INT). The snow SSL is .04m thick unless the snow thickness h_s is less than 0.08m, for which the snow SSL is half the layer thickness. The sea ice SSL is .05m for sea ice of total thickness h_i greater than 1.5m; for thinner sea ice the SSL is $h_i/30$. Fig A2 shows the thickness of the surface scattering layer for sea ice and how it varies with ice thickness h_i for three different thicknesses. Additionally, for the purposes of representing

refraction, we assume that between the SSL and DL sublayers in sea ice and at the pond surface for ponded sea ice (see Fig A1), an infinitesimally thin refractive boundary (see Fig A3). Fig A2 also shows (for three ice thicknesses) sea ice embedded in the ocean.

We take the four spectral/angle fluxes of Eq (A1) and cosine solar zenith angle μ_0, along with assumed underlying ocean albedos of $\alpha_{ovsdr} = \alpha_{ovsdf} = .01$ and $\alpha_{onidr} = \alpha_{onidf} = .0$, as adequate boundary conditions for solving for solar radiative transfer in the snow/pond/sea ice layers. Note we assume the four spectral/angle fluxes of Eq (A1) to be equally incident on each of the three general sufaces (Fig A1).

We use three spectral bands: vs $0.2 - 0.7$ μm, ni1 $0.7 - 1.19$ μm and ni2 $1.19 - 5.00$ μm, subdividing the near infrared band of the downwelling atmosphere shortwave to better represent near-infrared penetration below the surface. Thus, the F_{SWnidr} and F_{SWnidf} fluxes from the atmosphere are partitioned into the two near-infrared subbands as:

$$\begin{aligned} f_{ni} &= F_{SWnidr}/(F_{SWnidr} + F_{SWnidf}) \\ f_{ni1} &= 0.78 - 0.11 f_{ni} \\ f_{ni2} &= 1 - f_{ni1} \end{aligned} \tag{A3}$$

so that the diffuse flux in $ni1$, for example, is $f_{ni1} F_{SWnidf}$, and similarly for the other near-infrared fluxes and subbands.

Direct solar radiation is incident on all three surface types at cosine solar zenith angle μ_0. We assume the snow layer is granular, so that no change in solar beam zenith angle occurs in the snow layer. At the refractive boundary for pond surface and between SSL and DL for sea ice, refraction occurs. Thus the direct solar beam below the refractive boundary has cosine solar zenith angle μ_{0n} given by:

$$\mu_{0n} = \sqrt{1 - (1 - \mu_0^2)/n^2} \tag{A4}$$

where n is the index of refraction of pond water and sea ice relative to air. We assume a constant $n = 1.31$ (spectrally and vertically), for all layers below the refractive boundary, including the underlying ocean.

We assume all snow/pond/sea ice layers (Fig A1) and SSL,DL sublayers to be vertically and horizontally homogeneous, and futher to be spectrally homogeneous in each of the wave-bands mentioned above. Aerosols are mixed homogeneously with existing snow/pond/sea ice layers/sublayers.

We solve the multiple scattering problem for each snow/pond/sea ice column by separating layer multiple scattering from inter-layer multiple scattering. We do this by first evaluating the Delta-Eddington solutions for each layer, and then combining the layers to evaluate multiple scattering between them.

We consider each layer to be both absorbing and scattering. We specify the absorbing and scattering properties of each layer in terms of an absorption coefficient κ and a scattering

coefficient σ, whose sum is the extinction coefficient $k = \kappa + \sigma$. The single scattering albedo is the ratio of scattering to extinction, or $\omega = \sigma/(\kappa+\sigma)$, and the degree of forward/backward single scattering is given by the asymmetry parameter g. These last three properties (k, ω, g) are the inherent optical properties (IOPs) of the layer.

The radiative transfer equation for the plane-parallel, horizontally homogeneous scattering and absorbing layer is:

$$\mu \frac{dI}{d\tau} + I = \frac{\omega}{4\pi} \int_{4\pi} d\Omega' P(\Omega, \Omega') I(\Omega', \tau) \tag{A5}$$

with extinction optical depth of $\tau = 0$ at the layer upper boundary and $\tau = \tau_0$ at the lower layer boundary, with $\tau_0 = kz$, k is the extinction coefficient and z is the layer thickness, $\mu = cos\theta$ defined as positive for downward directed radiation and negative for upward directed radiation, I the intensity (or radiance), ω the single particle scattering albedo $(0 \leq \omega < 1)$, P the scattering phase function, and Ω the solid angle defined by the normalized direction vector. The intensity I represents the radiant energy per unit cross sectional area, per unit solid angle, and per unit time in a particular location and direction for each waveband.

We are interested only in radiative fluxes perpendicular to horizontal, namely up and down fluxes. Hence we use an azimuthally averaged form of Eq A5. Further, we represent strongly forward scattered phase function P as a delta-function δ and an Eddington approximation term, which in azimuthally averaged normalized form is:

$$P_{\delta E}(\mu) = 2f\delta(\mu - \mu') + (1-f)(1 + 3g^*\mu\mu') \tag{A6}$$

where δE refers to "Delta-Eddington", for scattering from zenith angles μ to μ', f is the forward scattered fraction, and g^* is a scaled asymmetry parameter $(g^* = (g-f)/(1-f))$. Finally, by using an embedded form of scattered direct solar radiation in each layer, Eq A5 becomes a scaled transfer equation in τ^*, ω^* (see Eq A9):

$$\mu \frac{dI}{d\tau^*} + I = \frac{\omega^*}{2} \int_{-1}^{+1} (1 + 3g^*\mu\mu') I \; d\mu' + \frac{\omega^* F_0}{4} (1 + 3g^*\mu_{0n}\mu) \; e^{-\tau^*/\mu_{0n}} \tag{A7}$$

where the direct beam solar appears as a single scattered source for diffuse radiation (second term R.H.S. of Eq. A7), with πF_0 the solar flux in the beam direction.

The single layer solution to this equation using the Eddington approximation for the layer reflectivity/transmissivity to direct radiation at angle μ_{0n} ($R(\mu_{0n})$, $T(\mu_{0n})$ respectively), and to diffuse radiation ($\overline{R}$, $\overline{T}$) respectively, is given by:

$$\begin{aligned}
R(\mu_{0n}) = \; & (\alpha-\gamma)(4u/N)e^{-\tau_0^*/\mu_{0n}} + (\alpha+\gamma)(u+1)(u-1)\left[e^{+\lambda\tau_0^*} - e^{-\lambda\tau_0^*}\right]/N - (\alpha-\gamma) \\
T(\mu_{0n}) = \; & (\alpha+\gamma)(4u/N) + (\alpha-\gamma)\left[\frac{(u+1)(u-1)(e^{+\lambda\tau_0^*} - e^{-\lambda\tau_0^*})}{N}\right] e^{-\tau_0^* \; /\mu_{0n}} \\
& - (\alpha+\gamma-1)e^{-\tau_0^*/\mu_{0n}} \\
\overline{R} = \; & 2\int_0^{+1} \mu R(\mu) \; d\mu \\
\overline{T} = \; & 2\int_0^{+1} \mu T(\mu) \; d\mu
\end{aligned} \tag{A8}$$

Table A1. Gaussian Angles and Weights. Angles are given as cosine of zenith angle μ.

number	μ	weight
1	.9894009	.0271525
2	.9445750	.0622535
3	.8656312	.0951585
4	.7554044	.1246290
5	.6178762	.1495960
6	.4580168	.1691565
7	.2816036	.1826034
8	.0950125	.1894506

with:

$$
\begin{aligned}
k &= \kappa + \sigma \\
\omega &= \sigma/(\kappa+\sigma) \\
f &= g^2 \\
\tau &= kz \\
\tau^* &= (1-\omega f)\tau \\
\omega^* &= \frac{(1-f)\omega}{1-\omega f} \\
g^* &= \frac{g-f}{1-f} \\
\lambda &= \sqrt{3(1-\omega^*)(1-\omega^* g^*)} \\
\alpha &= \frac{3}{4}\omega^* \mu_{0n}\left(\frac{1+g^*(1-\omega^*)}{1-\lambda^2\mu_{0n}^2}\right) \\
\gamma &= \frac{1}{2}\omega^*\left(\frac{1+3g^*(1-\omega^*)\mu_{0n}^2}{1-\lambda^2\mu_{0n}^2}\right) \\
u &= \frac{3}{2}\left(\frac{1-\omega^* g^*}{\lambda}\right) \\
N &= (u+1)^2 e^{\lambda\tau^*} - (u-1)^2 e^{-\lambda\tau^*}
\end{aligned}
\qquad (A9)
$$

where k, κ and σ are the extinction, absorption and scattering coefficients respectively, ω the single scattering albedo, f the forward scattered fraction, g the asymmetery parameter, τ the layer extinction optical depth, z the layer physical thickness, τ^*, ω^* and g^* scaled quantities, and λ,α,γ and N various solution terms. Again, $\mu_{0n} = \mu_0$ above the refractive boundary and Eq A4 below. The angular integrals in $\overline{R}$ and $\overline{T}$ are evaluated using the eight gaussian angles in Table A1.

As mentioned above, we treat the refractive boundary as an infinitesimally thin, non-absorbing sublayer with its own reflectivities/transmissivities ($R_f(\mu)$,$T_f(\mu)$,$\overline{R}_f$,$\overline{T}_f$). For un-

polarized radiation, the reflectivity/transmissivity to direct radiation at μ is:

$$\begin{aligned} R_f(\mu) &= \frac{1}{2}(R_1^2 + R_2^2) \\ R_1 &= \frac{\mu - n\mu_n}{\mu + n\mu_n} \\ R_2 &= \frac{n\mu - \mu_n}{n\mu + \mu_n} \\ T_f(\mu) &= 1 - R_f(\mu) \end{aligned} \tag{A10}$$

Using high angular resolution gaussian integration, we evalute the diffuse reflectivity/transmissivity to radiation from above (a) and below (b) for our assumed constant index of refraction $n = 1.31$ as:

$$\begin{aligned} \overline{R}_{fa} &= 0.063 \\ \overline{T}_{fa} &= 0.937 \\ \overline{R}_{fb} &= 0.455 \\ \overline{T}_{fb} &= 0.545 \end{aligned} \tag{A11}$$

Total internal reflection for angles less than critical below the refractive boundary causes the asymmetry in $\overline{R}_f$, $\overline{T}_f$ above and below the boundary. Fig A3 shows the refractive boundary for sea ice.

We assume inter-layer multiple scattering to be diffuse in the upward/downward hemispheres. Given a column of layer/sublayer reflectivities/transmissivities as in Eqs A8, A10, A11, we evalute inter-layer multiple scattering by combininig successive layers in pairs as in the following. For an arbitrary layer 1 with AOPs (apparent optical properties) $[R_1(\mu)\ T_1(\mu)\ \overline{R}_1\ \overline{T}_1]$ overlying layer 2 with AOPs $[R_2(\mu)\ T_2(\mu)\ \overline{R}_2\ \overline{T}_2]$, the combination formulas for direct and diffuse radiation incident from above are:

$$\begin{aligned} R_{12}(\mu) &= R_1(\mu) + \frac{\{(T_1(\mu) - Tdr_s)\overline{R}_2 + Tdr_s R_2(\mu)\}\overline{T}_1}{1 - \overline{R}_1\overline{R}_2} \\ T_{12}(\mu) &= Tdr_s T_2(\mu) + \frac{\{(T_1(\mu) - Tdr_s) + Tdr_s R_2(\mu)\overline{R}_1\}\overline{T}_2}{1 - \overline{R}_1\overline{R}_2} \\ \overline{R}_{12} &= \overline{R}_1 + \frac{\overline{T}_1\overline{R}_2\overline{T}_1}{1 - \overline{R}_1\overline{R}_2} \\ \overline{T}_{12} &= \frac{\overline{T}_1\overline{T}_2}{1 - \overline{R}_1\overline{R}_2} \end{aligned} \tag{A12}$$

with $Tdr_s = e^{-\tau_1^*/\mu}$ the direct solar beam transmission through layer 1, and the cosine solar zenith angle μ is μ_0 above the refractive boundary and μ_{0n} below the refractive boundary. The transmissions for each layer $[T_1(\mu_0)\ T_2(\mu_0)]$ and for the combined layers $[T_{12}(\mu_0)]$ are total transmissions, containing both direct and diffuse transmission.

For diffuse radiation from below the same two layers, the diffuse reflectivity/transmissivity $\overline{R}_{21}$ and $\overline{T}_{21}$ are evaluated as in Eq A12, except 1 and 2 are exchanged.

To combine the layers over the entire column, two vertical passes are made, one starting from the top and proceeding downward, the other starting from the specified ocean

surface reflectivities at the sea ice/ocean interface and proceeding upward. The result is that for every interface between layers/sublayers, the following combined reflectivities and transmissivities are available: Fdr_s, the direct beam flux transmission from the top to the interface, $R_{up}(\mu)$, the reflectivity to direct solar radiation of the entire column below the interface, $T_{dn}(\mu)$, the total transmission to direct solar radiation incident from the top to the interface, $\overline{R}_{up}$, the reflectivity of the column below the interface to diffuse radiation from above, $\overline{R}_{dn}$, the reflectivity of the column above the interface to diffuse radiation from below, and $\overline{T}_{dn}$, the transmissivity to diffuse radiation from the top to the interface. The resulting expressions for the downward and upward fluxes (normalized to 1) at every interface are:

$$\begin{aligned} Fdr_{dn} &= Fdr_s + \frac{(T_{dn}(\mu) - Fdr_s) + Fdr_s R_{up}(\mu)\overline{R}_{dn}}{1 - \overline{R}_{dn}\overline{R}_{up}} \\ Fdr_{up} &= \frac{Fdr_s R_{up}(\mu) + (T_{dn}(\mu) - Fdr_s)\overline{R}_{up}}{1 - \overline{R}_{dn}\overline{R}_{up}} \\ Fdf_{dn} &= \frac{\overline{T}_{dn}}{1 - \overline{R}_{dn}\overline{R}_{up}} \\ Fdf_{up} &= \frac{\overline{T}_{dn}\overline{R}_{up}}{1 - \overline{R}_{dn}\overline{R}_{up}} \end{aligned} \tag{A13}$$

where Fdr_s is the solar beam flux that transmits from the top to the interface, and again the cosine solar zenith angle μ is μ_0 above the refractive boundary and μ_{0n} below the refractive boundary.

Given the multiple scattering solutions within and between layers, the apparent optical properties (AOPs) of albedo, absorbed and transmitted flux can be evaluated. The surface albedos for direct and diffuse radiation are given by the band reflectivities $R_{up}(\mu_0)$, $\overline{R}_{up}$ at the top interface:

$$\begin{aligned} \alpha_{vsdr} &= R_{vsup}(\mu_0, top) \\ \alpha_{vsdf} &= \overline{R}_{vsup}(top) \\ \alpha_{nidr} &= R_{niup}(\mu_0, top) \\ \alpha_{nidf} &= \overline{R}_{niup}(top) \end{aligned} \tag{A14}$$

where *up* refers to reflectivities at the surface for solar radiation from above, and where *top* is the surface of snow, bare sea ice or pond. For the ni waveband, we first combine the two subband quantities using Eq (A3) before evaluating the ni reflectivites and fluxes. Thus, the spectral band (F_{SWvs}, F_{SWni}) and total column absorption (F_{SW}) can be evaluated as:

$$\begin{aligned} F_{SWvs} &= F_{SWvsdr}(1 - \alpha_{vsdr}) + F_{SWvsdf}(1 - \alpha_{vsdf}) \\ F_{SWni} &= F_{SWnidr}(1 - \alpha_{nidr}) + F_{SWnidf}(1 - \alpha_{nidf}) \\ F_{SW} &= F_{SWvs} + F_{SWni} \end{aligned} \tag{A15}$$

The visible and near-infrared surface (srf) absorption are:

$$\begin{aligned}
F_{SWvs-srf} =& \{Fdr_{vsdn}(top) - Fdr_{vsup}(top)\}F_{SWvsdr} + \{Fdf_{vsdn}(top) - Fdf_{vsup}(top)\}F_{SWvsdf} \\
&-\{Fdr_{vsdn}(bot) - Fdr_{vsup}(bot)\}F_{SWvsdr} - \{Fdf_{vsdn}(bot) - Fdf_{vsup}(bot)\}F_{SWvsdf} \\
F_{SWni-srf} =& \{Fdr_{nidn}(top) - Fdr_{niup}(top)\}F_{SWnidr} + \{Fdf_{nidn}(top) - Fdf_{niup}(top)\}F_{SWnidf} \\
&-\{Fdr_{nidn}(bot) - Fdr_{niup}(bot)\}F_{SWnidr} - \{Fdf_{nidn}(bot) - Fdf_{niup}(bot)\}F_{SWnidf}
\end{aligned} \tag{A16}$$

where we have added the spectral *vs* and *ni* to the up/down direct and diffuse fluxes of Eqs. A13, *top* is the pond surface (if present) as for the albedos above, and for snow and bare sea ice *top* is the top of the SSL, while *bot* is always the bottom of the SSL.

The INT layer absorptions (Q) are similar to those for the SSL, except *top* is the layer top interface, and *bot* is the layer bottom interface:

$$\begin{aligned}
Q_{SWvs} =& \{Fdr_{vsdn}(top) - Fdr_{vsup}(top)\}F_{SWvsdr} + \{Fdf_{vsdn}(top) - Fdf_{vsup}(top)\}F_{SWvsdf} \\
&-\{Fdr_{vsdn}(bot) - Fdr_{vsup}(bot)\}F_{SWvsdr} - \{Fdf_{vsdn}(bot) - Fdf_{vsup}(bot)\}F_{SWvsdf} \\
Q_{SWni} =& \{Fdr_{nidn}(top) - Fdr_{niup}(top)\}F_{SWnidr} + \{Fdf_{nidn}(top) - Fdf_{niup}(top)\}F_{SWnidf} \\
&-\{Fdr_{nidn}(bot) - Fdr_{niup}(bot)\}F_{SWnidr} - \{Fdf_{nidn}(bot) - Fdf_{niup}(bot)\}F_{SWnidf} \\
Q_{SW} =& Q_{SWvs} + Q_{SWni}
\end{aligned} \tag{A17}$$

Note that for the layer immediately under the SSL, the top of that layer for the flux difference calculation is the SSL/INT interface for snow and the SSL/DL interface for sea ice, as the flux absorbed above that interface is included in the surface absorption.

The spectral fluxes absorbed in the underlying ocean are:

$$\begin{aligned}
Q_{SWvs-ocn} =& \{Fdr_{vsdn}(ocn) - Fdr_{vsup}(ocn)\}F_{SWvsdr} + \{Fdf_{vsdn}(ocn) - Fdf_{vsup}(ocn)\}F_{SWvsdf} \\
Q_{SWni-ocn} =& \{Fdr_{nidn}(ocn) - Fdr_{niup}(ocn)\}F_{SWnidr} + \{Fdf_{nidn}(ocn) - Fdf_{niup}(ocn)\}F_{SWnidf} \\
Q_{SWocn} =& Q_{SWvs-ocn} + Q_{SWni-ocn}
\end{aligned} \tag{A18}$$

where *ocn* refers to the ocean/sea ice interface.

The albedos and fluxes of Eqs (A14-A18) are evaluated for each type of surface over the sea ice covered portion of a grid box, with fractions normalized to one as in Eq (A2). The fractions are set in the following fashion. When snow depth h_s is greater than .03m, snow is assumed to completely cover sea ice (i.e. $f_s = 1,\ f_i, f_p = 0$). When snow depth is less than .03m, we assume snow fraction is proportional to snow thickness. The remaining sea ice is either bare, or depending on the volume of melt water according to the melt pond parameterization, will have some non-zero fraction of ponds (i.e. $f_s = h_s/.03\text{m},\ f_i, f_p > 0$). If all snow cover melts, then only bare sea ice and ponded ice will have non-zero fractions (i.e. $f_s = 0,\ f_i, f_p > 0$).

The final sea ice averaged albedos and fluxes are thus given by:

$$\alpha = \alpha_s f_s + \alpha_i f_i + \alpha_p f_p \tag{A19}$$

$$F = F_s f_s + F_i f_i + F_p f_p \tag{A20}$$

where f_s is the horizontal coverage of snow over sea ice, f_i is the horizontal coverage of bare sea ice, f_p the horizontal coverage of melt ponds (for which the ponds completely cover underlying sea ice; see Fig. A1), α is the total albedo and $\alpha_s, \alpha_i, \alpha_p$ albedos of snow-covered, bare and ponded ice respectively, and F_s, F_i, F_p are the analogous fluxes.

It remains to tabulate the inherent optical properties (IOPs) of Eqs (A9), (k,ω,g) used to evaluate the layer multiple scattering solutions in Eqs (A8).

We represent snow as close packed (but independent) ice spheres whose IOPs are determined by the snow grain radius r_s. Assuming fixed snow density of $330kg\ m^{-2}$ and ice density of $917kg\ m^{-2}$, snow extinction, single scattering albedo and asymmetry parameters are given in Table A2 (expanded tables with more snow radii values are given in Briegleb and Light (2007)).

Because of the spectral averaging method used to determine the band average snow IOPs, the most accurate application of Table A2 is for clear sky. Cloudy sky alters the relative near-infrared spectrum (see Eq A3), such that for best comparison to benchmark calculations, snow grain radius must be reduced for overcast sky. Thus, the actual snow IOPs used are (subscript "s" refers to snow):

$$\begin{aligned} k_s &= k_s(r'_s) \\ \omega_s &= \omega_s(r'_s) \\ g_s &= g_s(r'_s) \\ r'_s &= f_r r_s \\ f_r &= 0.8 + 0.2 f_{ni} \end{aligned} \tag{A21}$$

where f_{ni} is from Eq (A3).

It remains to specify the snow grain radii actually used in CCSM4 sea ice radiation. Presently the snow grain radii minimum and maximum are set, with a temperature dependence near snow melting as follows:

$$\begin{aligned} r_s &= r_{s0} = \ 125\mu m \qquad T_s < -1.5C \\ r_s &= r_{s0} + (1500\mu m - r_{s0}) fT \qquad -1.5C < T_s < 0C \\ fT &= 1 + T_s/dT \\ dT &= 1.5C \end{aligned} \tag{A22}$$

where T_s is surface temperature in Celcius, fT is a weighting factor and dT is the temperature range below melting where the weighting factor is used. This is a rough approximation to represent snow grain growth due to aging and melting.

For bare sea ice and ponded sea ice, we use data and analysis inferred IOPs outlined extensively in Briegleb and Light (2007), as shown in the IOP Table A3. Ponded sea ice must have pond depth greater than $h_{p0} = 0.20$m to use the ponded ice IOPs. Pond depth h_p below .005m is considered bare ice. For pond depths inbetween these values, we linearly interpolate the scattering coefficient in pond depth between the bare ice and ponded ice values in Table A3 as:

$$\begin{aligned}
\sigma_i &= k_i\omega_i, \quad \sigma_p = k_p\omega_p \\
\kappa_p &= k_p(1-\omega_p) \\
\sigma(h_p) &= \sigma_i + (\sigma_p - \sigma_i)(h_p/h_{p0}) \\
k(h_p) &= \sigma(h_p) + \kappa_p \\
\omega(h_p) &= \sigma(h_p)/k(h_p) \\
g(h_p) &= g_i
\end{aligned} \tag{A23}$$

where subscript i refers to bare sea ice IOPs, and p refers to ponded sea ice IOPs. This is an approximate way of representing transitional water logging of the sea ice surface scattering layer as pond depth increases.

As mentioned previously, aerosols are mixed homogeneously with existing snow/pond/sea ice layers/sublayers (where the six types included are shown in the IOP table A4) in the following manner. Let the aerosol concentrations in a particular layer be $(q_n, n = 1, 6)$, where q is a mass mixing ratio and their individual IOPs be $(k_{an}, \omega_{an}, g_{an}, n = 1, 6)$. We consider the snow SSL for illustration of the mixing process. Let the snow SSL thickness be z_s, snow density ρ_s, and the snow SSL IOPs be (k_s,ω_s,g_s). Snow SSL extinction optical depth is $\tau_s = k_s z_s$. The total aerosol extinction optical depth and IOPs are given by:

$$\begin{aligned}
\tau_a &= (\Sigma_n k_{an} q_n)\ \rho_s z_s \\
\omega_a &= (\Sigma_n \omega_{an} k_{an} q_n)\rho_s z_s /\ \tau_a \\
g_a &= (\Sigma_n g_{an}\omega_{an} k_{an} q_n)\ \rho_s z_s /\ \omega_a \tau_a
\end{aligned} \tag{A25}$$

The total layer extinction optical depth τ, single scattering albedo ω and asymmetry parameter g are thus:

$$\begin{aligned}
\tau &= \tau_s\ +\ \tau_a \\
\omega &= (\omega_s\tau_s\ +\ \omega_a\tau_a)/(\tau_s\ +\ \tau_a) \\
g &= (g_s\omega_s\tau_s\ +\ g_a\omega_a\tau_a)/(\omega_s\tau_s\ +\ \omega_a\tau_a)
\end{aligned} \tag{A25}$$

Finally, though we include in these equations all six aerosols, in CCSM4 sea ice shortwave aerosols are limited to the hydrophilic and hydrophobic black carbon, and all dust (regardless of size range) is accumulated and uses the IOPs of the largest native dust size (see Table A4).

This completes the summary of the Sea Ice Delta-Eddington Shortwave algorithm.

Table A2. Snow extinction coefficients k_s, m^{-1}, for snow grain radii r_s.

$r_s(\mu m)$	$0.2-0.7\mu m$	$0.7-1.19\mu m$	$1.19-5.0\mu m$
50	10946.79	11008.69	11104.97
100	5445.56	5465.14	5495.33
200	2713.99	2720.17	2729.73
350	1548.18	1550.63	1554.39
500	1082.87	1084.21	1086.29
760	711.89	712.55	713.58
1000	540.83	541.26	541.91
2000	270.23	270.36	270.56
2500	216.15	216.24	216.38

Snow single scattering albedo ω_s, for snow grain radii r_s.

$r_s(\mu m)$	$0.2-0.7\mu m$	$0.7-1.19\mu m$	$1.19-5.0\mu m$
50	0.9999951	0.9997288	0.9751601
100	0.9999903	0.9994798	0.9621007
200	0.9999810	0.9990025	0.9444940
350	0.9999670	0.9983199	0.9256405
500	0.9999530	0.9976663	0.9101540
760	0.9999289	0.9965848	0.8865789
1000	0.9999068	0.9956323	0.8668233
2000	0.9998148	0.9919968	0.7968620
2500	0.9997691	0.9903277	0.7677887

Snow asymmetry parameter g_s, for snow grain radii r_s.

$r_s(\mu m)$	$0.2-0.7\mu m$	$0.7-1.19\mu m$	$1.19-5.0\mu m$
50	0.886931	0.887769	0.899072
100	0.889073	0.891127	0.910152
200	0.890238	0.893099	0.921540
350	0.890762	0.894123	0.930737
500	0.890975	0.894645	0.936148
760	0.891147	0.895212	0.941727
1000	0.891225	0.895601	0.944915
2000	0.891356	0.896851	0.951945
2500	0.891386	0.897399	0.954156

Table A3. Inherent Optical Properties of bare sea ice (k_i, ω_i, g_i, top three sets of rows) and ponded sea ice (k_p, ω_p, g_p, bottom three sets of rows). k is the extinction coefficient, ω the single scattering albedo, and g the asymmetry parameter. POND refers to pond water overlying sea ice, SSL to the sea ice surface scattering layer, DL to the sea ice drained layer, and INT to sea ice interior layers.

Level	$0.2-0.7\mu m$	$0.7-1.19\mu m$	$1.19-5.0\mu m$
bare ice	$k_i(\mathrm{m}^{-1})$	$k_i(\mathrm{m}^{-1})$	$k_i(\mathrm{m}^{-1})$
SSL	1000.1	1003.7	7042
DL	100.2	107.7	1309
INT	20.2	27.7	1445
	ω_i	ω_i	ω_i
SSL	.9999	.9963	.9088
DL	.9980	.9287	.0305
INT	.9901	.7223	.0277
	g_i	g_i	g_i
SSL	.94	.94	.94
DL	.94	.94	.94
INT	.94	.94	.94
ponded ice	$k_p(\mathrm{m}^{-1})$	$k_p(\mathrm{m}^{-1})$	$k_p(\mathrm{m}^{-1})$
POND	0.20	12	729
SSL	70.2	77.7	1309
DL	70.2	77.7	1309
INT	20.2	27.7	1445
	ω_p	ω_p	ω_p
POND	0	0	0
SSL	.9972	.9009	.0305
DL	.9972	.9009	.0305
INT	.9901	.7223	.0277
	g_p	g_p	g_p
POND	0	0	0
SSL	.94	.94	.94
DL	.94	.94	.94
INT	.94	.94	.94

Table A4. Inherent Optical Properties of aerosol. Six types of aerosol are shown: (1) hydrophobic black carbon, (2) hydrophilic black carbon, and four dust aerosols by particle size range: (3) 0.05-0.5 micro-meter, (4) 0.5-1.25 micro-meter, (5) 1.25-2.5 micro-meter, (6) 2.5-5.0 micro-meter. k is the extinction coefficient, ω the single scattering albedo, and g the asymmetry parameter. Note that in CCSM4 sea ice shortwave, the accumulated dust aerosol uses IOPs for aerosol number 6 in the table below.

Level	$0.2-0.7\mu m$	$0.7-1.19\mu m$	$1.19-5.0\mu m$
Type	k(m^2 kg^{-1})	k(m^2 kg^{-1})	k(m^2 kg^{-1})
1	11398.45	5446.82	2662.63
2	25368.61	11312.00	4467.60
3	2686.90	2220.84	750.33
4	841.09	1036.78	1106.79
5	387.85	414.18	459.02
6	196.64	204.36	218.65
	ω	ω	ω
1	0.28769	0.17060	0.06065
2	0.51595	0.41222	0.19629
3	0.97891	0.99397	0.96961
4	0.94375	0.98548	0.98663
5	0.90405	0.96555	0.97548
6	0.84982	0.94242	0.95433
	g	g	g
1	0.35023	0.19535	0.08230
2	0.52152	0.31925	0.13930
3	0.69091	0.70632	0.51110
4	0.69948	0.66296	0.71075
5	0.78564	0.73318	0.65122
6	0.82975	0.78243	0.74100

Figure A1. Types of snow/sea ice/pond surfaces used in the Delta-Eddington solar radiation treatment for sea ice, along with the vertical layering for each of these surfaces. The first type is snow of depth h_s with fractional coverage f_s that overlies sea ice. The second is bare sea ice with fractional coverage f_i. The third is ponded sea ice with fractional coverage f_p and ponds of depth h_p. The sea ice surface scattering layer thickness is $h_{1/4}$, the drained layer thickness just below the surface scattering layer is $h_{3/4} = h_i/4 - h_{1/4}$, where h_i is the total sea ice thickness, and the lowest three interior layers have thickness $h_i/4$. Snow and sea ice surface scattering layer (SSL) are stippled with large dots; the snow under its SSL is lightly stippled. Sea ice under pond is colored light gray, while pond is colored dark gray. Vertical dimensions are to relative scale for $h_i = 1.2$m, $h_s = .15$m and $h_p = .15$m, with both snow and sea ice SSL .04m thick.

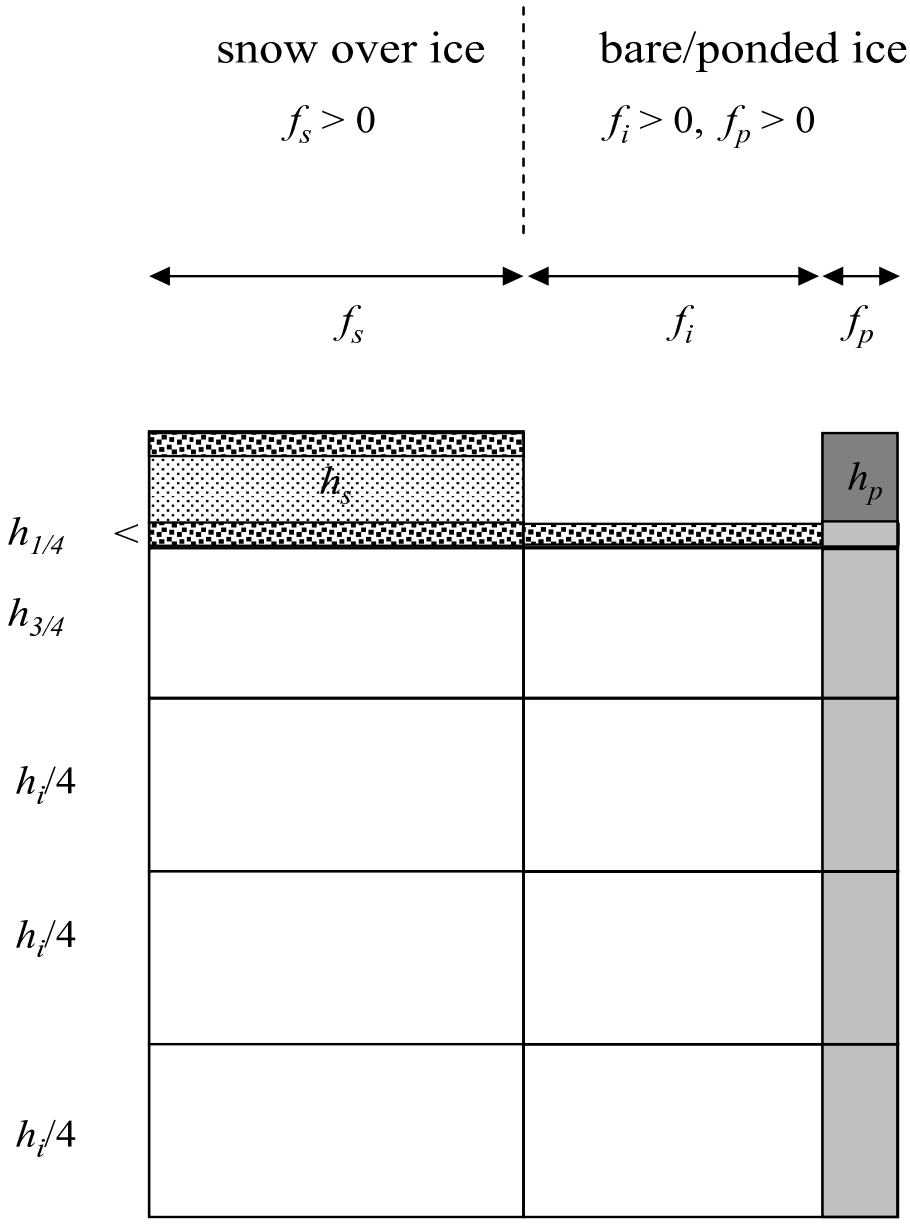

Figure A2. Sea ice layer structure, showing the surface scattering layer in relation to the drained layer and lower interior layers, for three sea ice thicknesses. h_i is the total sea ice thickness, with $h_i/4$ the thickness for the lowest three interior layers. The surface scattering layer thickness $h_{1/4}$ is $h_i/30$ for sea ice thinner than 1.50 m, and .05 m for thicker sea ice. The drained layer just below the surface scattering layer has thickness $h_{3/4} = h_i/4 - h_{1/4}$. Figure shown to scale, including sea ice freeboard.

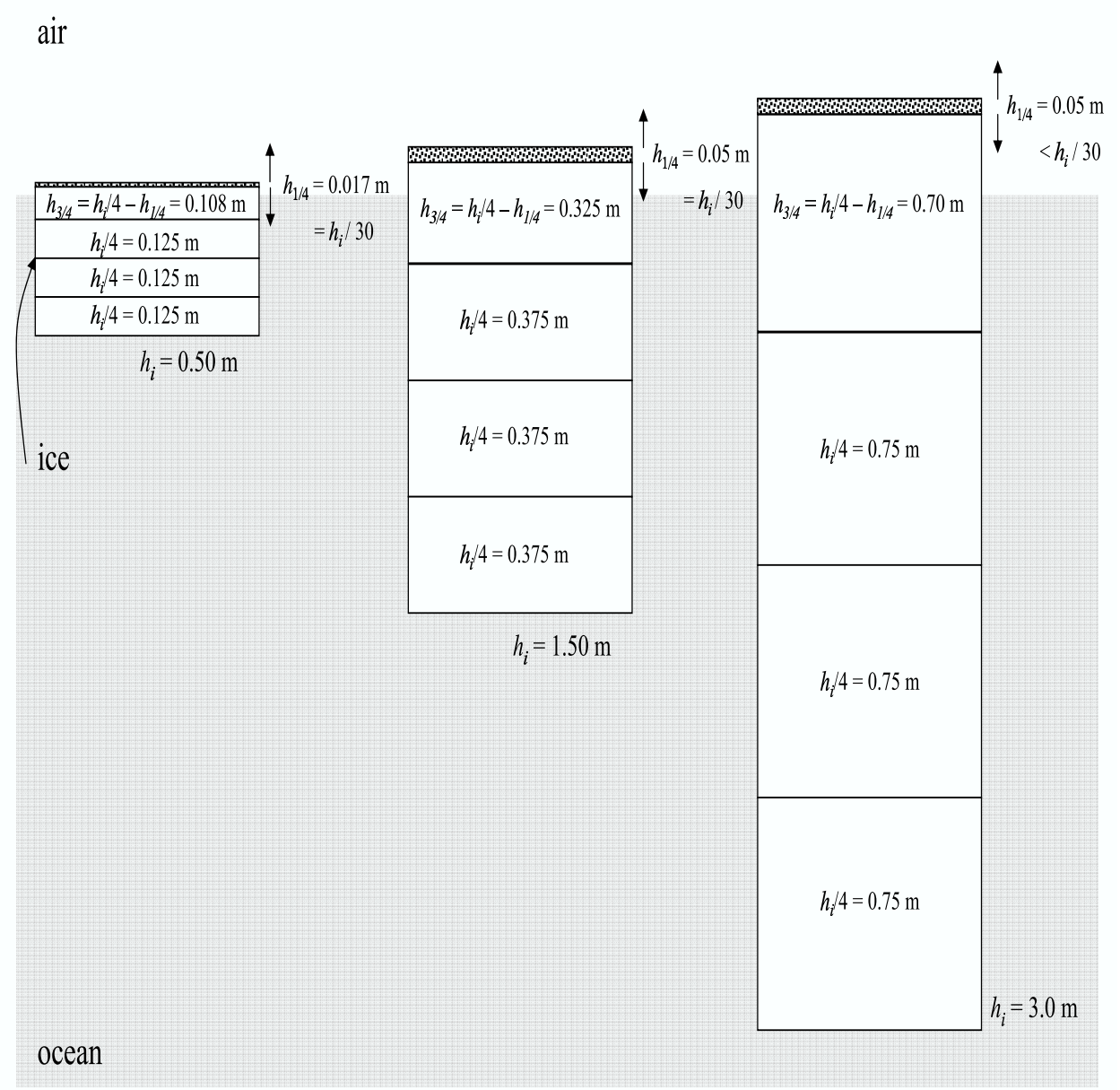

Figure A3. The refractive boundary location between the $h_{1/4}$ granular surface scattering layer and the $h_{3/4}$ solid drained layer in sea ice. A portion of the direct radiation at cosine zenith angle μ incident on the top of the sea ice transmits the $h_{1/4}$ surface scattering layer, is refracted by the refractive boundary into cosine zenith angle μ_n, and continues into the $h_{3/4}$ solid drained layer. The reflectivity and transmissivity to direct radiation at the refractive boundary are $R_f(\mu)$ and $T_f(\mu)$ respectively. The reflectivity and transmissivity to diffuse radiation from above the refractive boundary layer are $\overline{R}_{fa}$ and $\overline{T}_{fa}$ respectively, and from below the refractive layer $\overline{R}_{fb}$ and $\overline{T}_{fb}$ respectively.

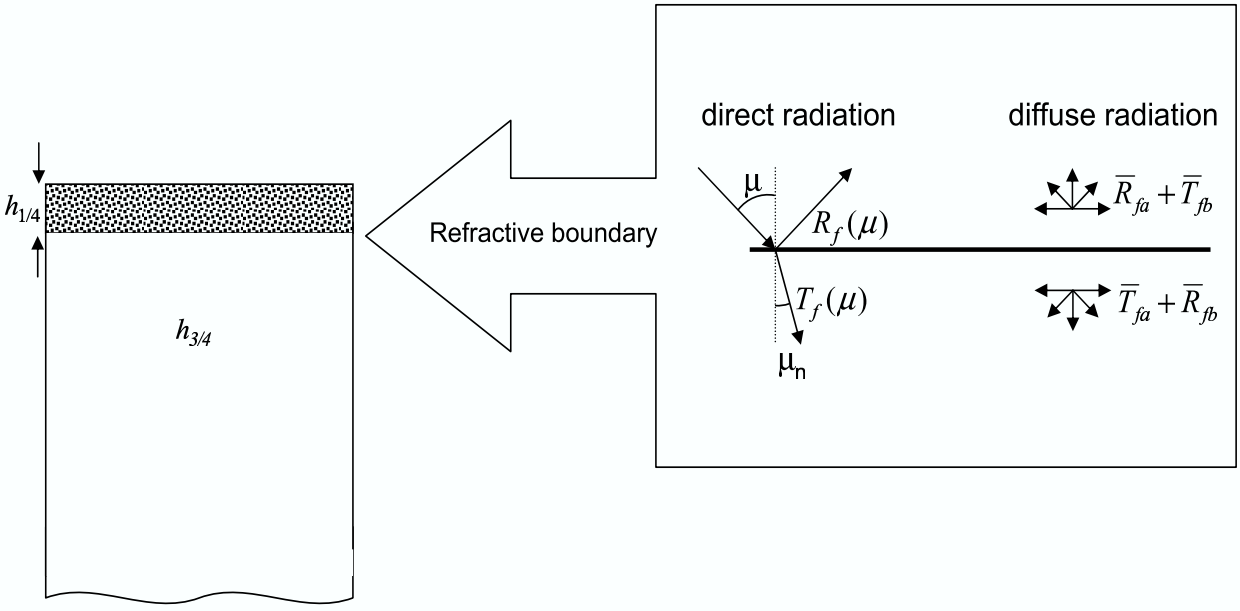

B. Comparison of CCSM4 Sea Ice Shortwave Radiation Albedos with Antarctic Measurements from Brandt et. al (2005)

1. Thick Snow on Antarctic Sea Ice

Brandt et. al (2005) has a very nice table (Table 3) of narrowband (vis, less than 0.7 micro-meters wavelength, and nir, greater than 0.7 micro-meters wavelength) albedo measurements for snow greater than 3cm thick on Antarctic sea ice, for seasons SON (September, October, November) and DJF (December, January, February). The paper suggests 50-100 micro-meter grain radii for fresh wind-blown snow, but 1000 micro-meter for melting surface snow grain radius, but otherwise no grain radii information is given along with the measured albedos. One might conjecture that for the SON period of southern spring, the snow grain radii will be small, order 50-200 micro-meters, while for the DJF southern summer, grain growth and/or some surface melt would increase grain radii to the 500-1000 micro-meter range. In Table B1 we have the albedos from Brandt et. al (2005), Table 3, for first year sea ice of thickness greater than 0.7m and with snow cover greater than 0.03m (i.e. thick snow).

Table B1. Comparison Thick Snow Waveband Albedos. The first row are the measurements of Brandt et. al (2005), while the remaining rows are calculated values from CCSM4 sea ice shortwave radiation for various snow radii r_s in micro-meters.

	VIS		NIR Clear		NIR Cloud	
r_s	SON	DJF	SON	DJF	SON	DJF
—	0.96	0.91	0.65	0.56	0.72	0.64
100	0.98		0.68		0.74	
150	0.98		0.65		0.71	
200	0.97		0.62		0.69	
300		0.97		0.59		0.65
400		0.96		0.56		0.62
500		0.95		0.54		0.60
1000		0.93		0.47		0.53
1500		0.91		0.43		0.49

We have compared these against CCSM4 sea ice radiation calculations. A one-dimensional version of CCSM4 sea ice radiation is used along with the polar atmosphere from Briegleb and Light (2007) to compute snow covered sea ice waveband albedos. Sea ice was 1.5m thick covered with 0.30m snow of specified snow grain radius. We ran both clear sky and completely overcast (cloud) cases for a range of snow grain radii. Note that we used the

0.80 reduction factor in snow grain radius for cloudy sky as discussed in Briegleb and Light (2007) and in Part A of this Supplemental Material.

For clear sky early in the season (SON) with smaller snow grain radii, the comparison shows reasonable agreement (i.e. within .02 absolute) in the wave band albedos for a range of snow grain radii 100-200 micro-meters. The results for cloudy sky also bracket the measurements. Overall, 150 micro-meter grain radii give the best comparison. Also note that the change in nir from clear to cloudy (0.06-0.07) with cloudy sky nir albedo larger, is nearly the same as the 0.07 change in the measurements, and in the same direction.

For the summer season (DJF), we see that the best fit for the near infrared is for grain radii between 300 to 500 micro-meters, with 400 micro-meters being the best. We note the observations give a 0.08 increase in nir albedo for cloudy sky, while the CCSM4 sea ice radiation only gives .06, though again in the same direction. The visible band albedos are .04-.06 too high though, and while using 1000 micro-meter grain radius brings this difference down to only .02, the corresponding nir albedos are significantly lower than the observed.

We now compare the corresponding broad band or all-wave albedos.

Table B2. Comparison Thick Snow All-Wave Albedos. The first row are the measurements of Brandt et. al (2005), while the remaining rows are calculated values from CCSM4 sea ice shortwave radiation for various snow radii r_s in micro-meters.

	SON		DJF	
	Clear	Cloud	Clear	Cloud
—	0.81	0.87	0.75	0.81
150	0.82	0.89		
200	0.80	0.87		
400			0.77	0.85
500			0.75	0.84
1000			0.71	0.80

These broad band all-wave comparisons are fairly good.

Both all-wave and narrow band comparisons, apart from melt season visible albedo (because of melt water or contaminants?), show that the CCSM4 sea ice shortwave radiation is able to simulate snow spectral albedo fairly well for an appropriate range of snow grain radii and for clear as well as cloudy sky.

2. Bare Antarctic Sea Ice

Here we consider bare sea ice (i.e. no snow) cases of Brandt et al. (2005). We compare measured albedos against CCSM4 sea ice shortwave radiation. For the latter, the SSL physical thickness is set to be sea ice thickness over 30, or approximately 1/3 of freeboard, but otherwise uses the same IOPs as for thick sea ice (1.5m) for which SHEBA measurements were used. We note that the surface bare sea ice melting layer may not have the same structure as that of thin un-melted sea ice. Brandt et. al (2005) note that when grease ice forms nilas of a few centimeters thick its structure has "randomly oriented oriented crystals" that have "a high concentration of bubble and brine inclusions". CCSM4 sea ice radiation's simple assumption of a thinning (in proportion to ice thickness) SSL appropriate for thicker melting sea ice surface is surely a rough approximation that does allow enhanced scattering in the SSL, but possibly not represent all of the complex structure of true thin un-melted sea ice.

We now compare all-wave and waveband albedos.

Table B3. Brandt et. al (2005) measured albedos (top rows) for Antarctic Bare Sea Ice, where BB stands for 'broad band' (all-wave), ygi stands for 'young grey ice', ygwi for 'young grey white ice', and fyi for 'first year ice', and CCSM4 sea ice shortwave radiation computed albedos for bare sea ice (bottom rows).

		BB		VIS		NIR	
		Clear	Cloud	Clear	Cloud	Clear	Cloud
Ice Type	Thickness (cm)						
ygi	10-15	0.25	0.27	0.30	0.30	0.19	0.21
ygwi	15-30	0.32	0.34	0.39	0.39	0.23	0.25
fyi	30-70	0.41	0.45	0.54	0.54	0.27	0.29
fyi	>70	0.49	0.54	0.67	0.67	0.29	0.31
—	10	0.24	0.24	0.28	0.27	0.21	0.20
—	15	0.30	0.29	0.35	0.33	0.25	0.23
—	20	0.34	0.33	0.41	0.38	0.27	0.26
—	30	0.40	0.39	0.49	0.46	0.31	0.30
—	40	0.44	0.44	0.55	0.51	0.34	0.33
—	50	0.48	0.48	0.59	0.56	0.36	0.36
—	70	0.53	0.53	0.65	0.62	0.39	0.39
—	140	0.60	0.64	0.76	0.74	0.43	0.45

We have included a range of sea ice thicknesses to try to bracket the measurements. Careful examination suggests that the best fits overall for the observed ice type categories are given

in Table B4.

Table B4. Best fit CCSM4 sea ice thicknesses to the Brandt et. al (2005) measured albedos for Antarctic Bare Sea Ice.

Ice Type	Thickness (cm)
ygi	10
ygwi	20
fyi	40
fyi	70

Broadband albedo differences for these best fits are order .01 to .02, while waveband albedo differences are larger, especially in the near-ir with CCSM4 larger up to .07 . Also, CCSM4 thicknesses for these best fits tend to be on the low end of the thickness range of the measurements.

As just mentioned, CCSM4 tends to have somewhat smaller vis and larger nir waveband albedos than the measurements. Also, the clear to cloudy sky differences in all-wave albedo for the measurements show increases with cloudy sky compared to clear sky, while the thinner sea ice in CCSM4 has the opposite tendency. The latter is probably due to the zenith angle dependence of the surface scattering: clear sky has much more direct radiation which generally has a higher albedo for low sun that would the cloudy sky diffuse radiation. Such an effect does not seem to be present in the measurements however. In the CCSM4 sea ice radiation calculations the solar zenith angle is fixed at 60 degrees (30 degree elevation angle), while the measurements will undoubtedly have a range of solar elevation angles.

References

Brandt, R.E., S.G.Warren, A.P.Worby and T.C.Grenfell, 2005: "Surface Albedo of the Antarctic Sea Ice Zone" J.of Climate 18 3606-3622

Briegleb, B.P. and B. Light, 2007: A Delta-Eddington Multiple Scatterin Parameterization for Solar Radiation in the Sea Ice Component of the Community Climate System Model. NCAR Tech Note, TN-472+STR, 100pp.